Dual electro-optical modulator polarimeter based on adaptive optics scanning laser ophthalmoscope

Hongxin Song, Xiaofeng Qi, Weiyao Zou, Zhangyi Zhong, and Stephen A. Burns*

School of Optometry, Indiana University, 800 East Atwater avenue, Bloomington, IN, 47405, USA
**staburns@indiana.edu*

Abstract: We constructed a high speed and high-resolution Stokes vector retinal imaging polarimeter with dual electro-optical modulators based on adaptive optics scanning laser ophthalmoscope. By varying the voltages on the EO crystals line by line, we were able to measure over 500,000 Stokes vectors per second. We used this system in three human subjects demonstrating the capability of the system to be employed *in vivo*. The high speed effectively decreases the adverse impact of eye motion induced errors in polarization calculations, improving the contrast of retinal structures based on their polarization properties.

OCIS codes: (120.3890) Medical optics instrumentation; (170.4460) Ophthalmic optics and devices; (180.1790) Confocal microscopy; (330.4300) Vision system - noninvasive assessment.

References and links

1. L. J. Bour, "Polarized Light and the Eye," *Visual Optics and Instrumentation* **1**, (1991).
2. G. J. Van Blokland, and S. C. Verhelst, "Corneal polarization in the living human eye explained with a biaxial model," J. Opt. Soc. Am. A **4**(1), 82–90 (1987).
3. D. S. Greenfield, R. W. Knighton, and X. R. Huang, "Effect of corneal polarization axis on assessment of retinal nerve fiber layer thickness by scanning laser polarimetry," Am. J. Ophthalmol. **129**(6), 715–722 (2000).
4. R. N. Weinreb, C. Bowd, D. S. Greenfield, L. M. Zangwill, and M. Zangwill, "Measurement of the magnitude and axis of corneal polarization with scanning laser polarimetry," Arch. Ophthalmol. **120**(7), 901–906 (2002).
5. L. J. Bour, and N. J. Lopes Cardozo, "On the birefringence of the living human eye," Vision Res. **21**(9), 1413–1421 (1981).
6. X.-R. Huang, and R. W. Knighton, "Microtubules contribute to the birefringence of the retinal nerve fiber layer," Invest. Ophthalmol. Vis. Sci. **46**(12), 4588–4593 (2005).
7. J. M. Gorrand, R. Alfieri, and J. Y. Boire, "Diffusion of the retinal layers of the living human eye," Vision Res. **24**(9), 1097–1106 (1984).
8. A. W. Dreher, and K. Reiter, "Retinal Laser Ellipsometry - a New Method for Measuring the Retinal Nerve-Fiber Layer Thickness Distribution," Clin. Vis. Sci. **7**, 481–488 (1992).
9. J. Sjöstrand, Z. Popovic, N. Conradi, and J. Marshall, "Morphometric study of the displacement of retinal ganglion cells subserving cones within the human fovea," Graefes Arch. Clin. Exp. Ophthalmol. **237**(12), 1014–1023 (1999).
10. G. J. van Blokland, "Ellipsometry of the human retina in vivo: preservation of polarization," J. Opt. Soc. Am. A **2**(1), 72–75 (1985).
11. H. B. Brink, and G. J. van Blokland, "Birefringence of the human foveal area assessed in vivo with Mueller-matrix ellipsometry," J. Opt. Soc. Am. A **5**(1), 49–57 (1988).
12. A. E. Elsner, A. Weber, M. C. Cheney, and D. A. Vannasdale, "Spatial distribution of macular birefringence associated with the Henle fibers," Vision Res. **48**(26), 2578–2585 (2008).
13. M. Pircher, E. Götzinger, R. Leitgeb, H. Sattmann, O. Findl, and C. K. Hitzenberger, "Imaging of polarization properties of human retina in vivo with phase resolved transversal PS-OCT," Opt. Express **12**(24), 5940–5951 (2004).
14. D. A. VanNasdale, A. E. Elsner, A. Weber, M. Miura, and B. P. Haggerty, "Determination of foveal location using scanning laser polarimetry," J. Vis. **9**(3), 21, 1–17 (2009).
15. J. M. Bueno, "Depolarization effects in the human eye," Vision Res. **41**(21), 2687–2696 (2001).
16. J. M. Bueno, J. J. Hunter, C. J. Cookson, M. L. Kisilak, and M. C. W. Campbell, "Improved scanning laser fundus imaging using polarimetry," J. Opt. Soc. Am. A **24**(5), 1337–1348 (2007).
17. B. Cense, T. C. Chen, B. H. Park, M. C. Pierce, and J. F. de Boer, "In vivo birefringence and thickness measurements of the human retinal nerve fiber layer using polarization-sensitive optical coherence tomography," J. Biomed. Opt. **9**(1), 121–125 (2004).

#132430 - $15.00 USD Received 29 Jul 2010; revised 18 Sep 2010; accepted 19 Sep 2010; published 30 Sep 2010

18. K. M. Twietmeyer, R. A. Chipman, A. E. Elsner, Y. Zhao, and D. VanNasdale, "Mueller matrix retinal imager with optimized polarization conditions," Opt. Express **16**(26), 21339–21354 (2008).
19. J. M. Bueno, and P. Artal, "Polarization and retinal image quality estimates in the human eye," J. Opt. Soc. Am. A **18**(3), 489–496 (2001).
20. C. K. Hitzenberger, E. Goetzinger, M. Sticker, M. Pircher, and A. F. Fercher, "Measurement and imaging of birefringence and optic axis orientation by phase resolved polarization sensitive optical coherence tomography," Opt. Express **9**(13), 780–790 (2001).
21. M. Pircher, E. Götzinger, O. Findl, S. Michels, W. Geitzenauer, C. Leydolt, U. Schmidt-Erfurth, and C. K. Hitzenberger, "Human macula investigated in vivo with polarization-sensitive optical coherence tomography," Invest. Ophthalmol. Vis. Sci. **47**(12), 5487–5494 (2006).
22. M. C. Cheney, A. E. Elsner, S. A. Burns, M. B. M. Kairala, C. L. Trempe, K. Lashkari, J. J. Weiter, M. Miura, M. Osako, and M. Usui, "Polarization amplitude and phase changes in retinal exudation," Invest. Ophthalmol. Vis. Sci. **44**, U691–U691 (2003).
23. A. E. Elsner, M. Miura, J. B. Stewart, M. B. M. Kairala, and S. A. Burns, "Novel algorithms for polarization imaging resulting in improved quantification of retinal blood vessels.," in *Medicine Meets Virtual Reality*, J. D. Westwood, ed. (IOS Press, Washington, D.C., 2003), pp. 59–61.
24. M. B. Mellem-Kairala, A. E. Elsner, A. Weber, R. B. Simmons, and S. A. Burns, "Improved contrast of peripapillary hyperpigmentation using polarization analysis," Invest. Ophthalmol. Vis. Sci. **46**(3), 1099–1106 (2005).
25. R. N. Weinreb, C. Bowd, and L. M. Zangwill, "Glaucoma detection using scanning laser polarimetry with variable corneal polarization compensation," Arch. Ophthalmol. **121**(2), 218–224 (2003).
26. M. T. Nicolela, C. Martinez-Bello, C. A. Morrison, R. P. LeBlanc, H. G. Lemij, T. P. Colen, and B. C. Chauhan, "Scanning laser polarimetry in a selected group of patients with glaucoma and normal controls," Am. J. Ophthalmol. **132**(6), 845–854 (2001).
27. S. A. Burns, A. E. Elsner, M. B. Mellem-Kairala, and R. B. Simmons, "Improved contrast of subretinal structures using polarization analysis," Invest. Ophthalmol. Vis. Sci. **44**(9), 4061–4068 (2003).
28. C. Ahlers, E. Götzinger, M. Pircher, I. Golbaz, F. Prager, C. Schütze, B. Baumann, C. K. Hitzenberger, and U. Schmidt-Erfurth, "Imaging of the retinal pigment epithelium in age-related macular degeneration using polarization-sensitive optical coherence tomography," Invest. Ophthalmol. Vis. Sci. **51**(4), 2149–2157 (2010).
29. S. Michels, M. Pircher, W. Geitzenauer, C. Simader, E. Götzinger, O. Findl, U. Schmidt-Erfurth, and C. K. Hitzenberger, "Value of polarisation-sensitive optical coherence tomography in diseases affecting the retinal pigment epithelium," Br. J. Ophthalmol. **92**(2), 204–209 (2008).
30. M. Miura, M. Yamanari, T. Iwasaki, A. E. Elsner, S. Makita, T. Yatagai, and Y. Yasuno, "Imaging polarimetry in age-related macular degeneration," Invest. Ophthalmol. Vis. Sci. **49**(6), 2661–2667 (2008).
31. A. Weber, M. C. Cheney, Q. Y. J. Smithwick, and A. E. Elsner, "Polarimetric imaging and blood vessel quantification," Opt. Express **12**(21), 5178–5190 (2004).
32. M. Miura, A. E. Elsner, M. C. Cheney, M. Usui, and T. Iwasaki, "Imaging polarimetry and retinal blood vessel quantification at the epiretinal membrane," J. Opt. Soc. Am. A **24**(5), 1431–1437 (2007).
33. T. Y. Chui, H. Song, and S. A. Burns, "Adaptive-optics imaging of human cone photoreceptor distribution," J. Opt. Soc. Am. A **25**(12), 3021–3029 (2008).
34. T. Y. P. Chui, H. Song, and S. A. Burns, "Individual variations in human cone photoreceptor packing density: variations with refractive error," Invest. Ophthalmol. Vis. Sci. **49**(10), 4679–4687 (2008).
35. A. Roorda, F. Romero-Borja, W. Donnelly Iii, H. Queener, T. J. Hebert, and M. C. W. Campbell, "Adaptive optics scanning laser ophthalmoscopy," Opt. Express **10**(9), 405–412 (2002).
36. A. Roorda, Y. H. Zhang, and J. L. Duncan, "High-resolution in vivo imaging of the RPE mosaic in eyes with retinal disease," Invest. Ophthalmol. Vis. Sci. **48**(5), 2297–2303 (2007).
37. D. C. Gray, W. Merigan, J. I. Wolfing, B. P. Gee, J. Porter, A. Dubra, T. H. Twietmeyer, K. Ahamd, R. Tumbar, F. Reinholz, and D. R. Williams, "In vivo fluorescence imaging of primate retinal ganglion cells and retinal pigment epithelial cells," Opt. Express **14**(16), 7144–7158 (2006).
38. Z. Zhong, B. L. Petrig, X. Qi, and S. A. Burns, "In vivo measurement of erythrocyte velocity and retinal blood flow using adaptive optics scanning laser ophthalmoscopy," Opt. Express **16**(17), 12746–12756 (2008).
39. J. A. Martin, and A. Roorda, "Direct and noninvasive assessment of parafoveal capillary leukocyte velocity," Ophthalmology **112**(12), 2219–2224 (2005).
40. H. Song, Y. Zhao, X. Qi, Y. T. Chui, and S. A. Burns, "Stokes vector analysis of adaptive optics images of the retina," Opt. Lett. **33**(2), 137–139 (2008).
41. B. Wang, A. Leadbetter, and R. R. Rockwell, "Evaluation of a dual PEM Stokes polarimeter using different signal processing methods," J. A. Shaw, and J. S. Tyo, eds. (SPIE, San Diego, CA, USA, 2005), pp. 58880W–58888.
42. S. A. Burns, R. Tumbar, A. E. Elsner, D. Ferguson, and D. X. Hammer, "Large-field-of-view, modular, stabilized, adaptive-optics-based scanning laser ophthalmoscope," J. Opt. Soc. Am. A **24**(5), 1313–1326 (2007).
43. W. A. Shurcliff, "Polarized Light: Production and Use," Harvard U. Press (1962).
44. R. A. Chipman, "Polarimetry," *Handbook of Optics* **2**, 22.21–22.37 (1995).
45. S. B. Stevenson, and A. Roorda, "Correcting for Miniature Eye Movements in High Resolution Scanning Laser Ophthalmoscopy," Proc. SPIE **5688A**, 145–151 (2005).
46. A. E. Elsner, A. Weber, M. C. Cheney, D. A. VanNasdale, and M. Miura, "Imaging polarimetry in patients with neovascular age-related macular degeneration," J. Opt. Soc. Am. A **24**(5), 1468–1480 (2007).
47. M. Miura, A. E. Elsner, A. Weber, M. C. Cheney, M. Osako, M. Usui, and T. Iwasaki, "Imaging polarimetry in central serous chorioretinopathy," Am. J. Ophthalmol. **140**(6), 1014–1019 (2005).

#132430 - $15.00 USD Received 29 Jul 2010; revised 18 Sep 2010; accepted 19 Sep 2010; published 30 Sep 2010

48. J. M. Bueno, "Measurement of parameters of polarization in the living human eye using imaging polarimetry," Vision Res. **40**(28), 3791–3799 (2000).
49. T. A. Maldonado, "Electro-optics Modulators," *Handbook of Optics* **2**, 13.11–13.35 (1995).
50. R. W. Knighton, and X. R. Huang, "Linear birefringence of the central human cornea," Invest. Ophthalmol. Vis. Sci. **43**(1), 82–86 (2002).
51. G. J. Van Blokland, and S. C. Verhelst, "Corneal polarization in the living human eye explained with a biaxial model," J. Opt. Soc. Am. A **4**(1), 82–90 (1987).
52. R. N. Weinreb, C. Bowd, D. S. Greenfield, and L. M. Zangwill, "Measurement of the magnitude and axis of corneal polarization with scanning laser polarimetry," Arch. Ophthalmol. **120**(7), 901–906 (2002).
53. W. S. Stiles, and B. H. Crawford, "The luminous efficiency of rays entering the eye pupil at different points," Proc. R. Soc. Lond. **112**(778), 428–450 (1933).
54. G. T. D. Francia, "Retinal cones as dielectric antennas," J. Opt. Soc. Am. **39**(4), 324 (1949).
55. A. W. Snyder, and C. Pask, "The Stiles-Crawford effect--explanation and consequences," Vision Res. **13**(6), 1115–1137 (1973).
56. W. Gao, B. Cense, Y. Zhang, R. S. Jonnal, and D. T. Miller, "Measuring retinal contributions to the optical Stiles-Crawford effect with optical coherence tomography," Opt. Express **16**(9), 6486–6501 (2008).
57. G. J. van Blokland, and D. van Norren, "Intensity and polarization of light scattered at small angles from the human fovea," Vision Res. **26**(3), 485–494 (1986).
58. S. A. Burns, S. Wu, F. C. Delori, and A. E. Elsner, "Direct measurement of human-cone-photoreceptor alignment," J. Opt. Soc. Am. A **12**(10), 2329–2338 (1995).

1. Introduction

The polarization state of light scattered from tissue is controlled by both the properties of the medium through which the light travels to and from the tissue and by the structural and optical properties of the tissue itself. The human eye, for example, has complex polarization properties that vary as light traverses the eye from the cornea to the retina. An approximately fixed retardation was found at the central area of the cornea, although there are spatial variations [1–4]. The crystalline lens has a lamellar organization of lenticular cells, but unlike the cornea, does not contribute substantially to the total optical retardation of the eye [2,5]. The retinal nerve fiber layer (RNFL) is composed of the ganglion cell axons and exhibits birefringence arising from the organization of microtubules [5–10] as do the Henle fibers [11–14].

Polarization techniques have been used in measuring and visualizing the structures of healthy eyes [13,15–21] as well as diseased eyes [22–24]. Scanning laser polarimetry (SLP) is used clinically as an aid to diagnose and to monitor glaucoma by measuring the retardation of the RNFL [25,26] as an estimator of nerve fiber layer thickness. Polarization can also be used to improve the contrast of pathological subretinal structures by removing the polarization retaining light from the depolarized or randomly polarized light [27]. It can quantitatively detect retinal changes associated with aging, age-related maculopathy and macular degeneration [27–30], as well as retinal blood vessels [31,32].

Adaptive optics scanning laser ophthalmoscopes (AOSLO) have been used in human retinal imaging of cone photoreceptors [33–35], RPE cells [36,37] and capillaries [38,39]. In a previous study, we developed an AOSLO polariscope and demonstrated that the polarization properties of the retina can be measured at the cellular level [40]. The previous polarization AOSLO was built by introducing a quarter wave plate and a polarizer in the detection channel. However, the system had several drawbacks. For instance, it took about 30 minutes to acquire a set of retinal images for analyzing the polarization properties of one small area of the retina. The retinal images were very dim when the quarter wave plate was at certain angles, making it difficult to align and average images from those angles in post-processing. In addition, intensity fluctuations over time, arising from both variations in tear film, AO correction quality, and eye movements introduced errors into the computation. In the present study, we present a new technique where we couple our AOSLO detector to dual electro-optical modulators (Lithum Niobate, LiNbO3) and a polarizer using an approach similar to one using photoelastic modulators [41]. With this new system, we were able to measure over 500,000 Stokes Vectors per second. The high speed decreases the impact of eye motion induced alignment errors. It provides a more efficient approach for studying the polarization properties of the retina at the cellular level.

#132430 - $15.00 USD Received 29 Jul 2010; revised 18 Sep 2010; accepted 19 Sep 2010; published 30 Sep 2010

2. Method

2.1 Apparatus

We modified the Indiana adaptive optics SLO [42] as shown in Fig. 1. A flip mirror (FM1) is introduced into the detection channel after the confocal apertures. By inserting or removing this mirror, we can rapidly switch between regular retinal imaging and polarization imaging. A lens (f = 30 mm) collimates and shrinks the beam diameter to 1.5 mm. A second flip mirror (FM2) is used to switch between channel A and channel B. Channel A is the high speed channel, consisting of two electro-optical crystals (Lithium Niobate, LiNbO3) and a polarizer (Corning PolarCor) followed by a detector (APD Perkins Elmer). The fast axis of the first and second crystal and the polarizer was 0, 45, and 90 degrees relative to the table plane respectively. The apertures of the two crystals are both 2 mm. Channel B is the slower, waveplate based system, which consists of a rotatable high quality quarter wave plate, a polarizer and a detector. This channel was used for calibrating the polarization properties of channel A.

The imaging light source was a superluminescent diode (SLD, Superlum, Russia) with a 15 nm bandwidth centered at 830 nm. A half-wave plate was used to control the polarization of the incident light. Corneal power of the imaging beam was 320 μW. Wavefront sensing was performed using a custom Shack-Hartman sensor (SHS) consisting of a 12-bit CCD cameralink camera (Uniq Vision 1820) and a precision lenslet array (Adaptive Optics Associates). The wavefront sensing beacon was provided by a 680 nm SLD with 50 μW input into the eye. During polarization imaging, the imaging field size was smaller because we scanned the same line of the retina 7 times while we changed the voltages on the two EO crystals before moving to the next line. However, total power was still more than 10 times below ANSI safe exposure level for all field sizes and durations used.

2.2 Device calibration

2.2.1 Calibration of the EO crystals based on ideal Mueller matrix

The polarization state of a light beam can be described by a four-element column vector, $[S_0 \quad S_1 \quad S_2 \quad S_3]^T$, known as a Stokes vector [43], where S_0 represents the total intensity of the light, S_1 the difference between horizontal and vertical linear components, S_2 the difference between + 45° and −45° linear components, and S_3 the difference between right and left circular components. The degree of polarization (DOP) [44] is the proportion of light that is polarized, while the degree of depolarization (DODP) is 1-DOP.

The retardation of an optical element can be described by a Mueller matrix [44]. Therefore the theoretical Mueller matrix of the LiNbO3 crystals can be written as

$$M = \begin{bmatrix} 1 & 0 & 0 & 0 \\ 0 & \cos^2 2\theta + \sin^2 2\theta \cos\sigma & \sin 2\theta \cos 2\theta (1-\cos\sigma) & -\sin 2\theta \sin\sigma \\ 0 & \sin 2\theta \cos 2\theta (1-\cos\sigma) & \sin^2 2\theta + \cos^2 2\theta \cos\sigma & \cos 2\theta \sin\sigma \\ 0 & \sin 2\theta \sin\sigma & -\cos 2\theta \sin\sigma & \cos\sigma \end{bmatrix} \quad (1)$$

where θ is the angle of the fast axis of the crystal and σ is its birefringence. If the half-wave voltage of the crystal is V_π, the birefringence σ when voltage V is applied is

$$\sigma = \frac{V \cdot \pi}{V_\pi} \quad (2)$$

#132430 - $15.00 USD Received 29 Jul 2010; revised 18 Sep 2010; accepted 19 Sep 2010; published 30 Sep 2010

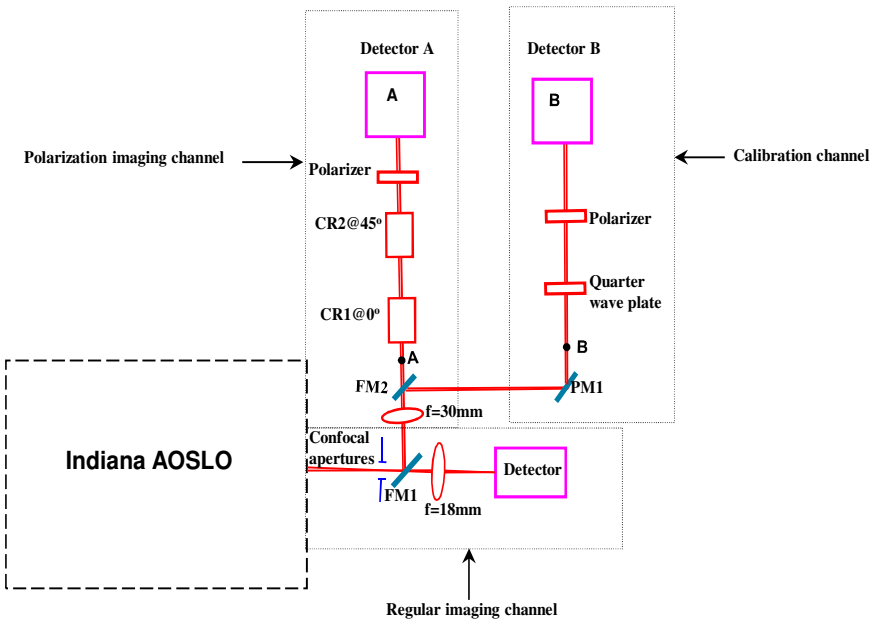

Fig. 1. Schematic of the AOSLO polarimeter. Channel A with dual LiNbO3 crystals (CR1 and CR2) is for polarization imaging. Channel B is used to calibrate the dual crystals in Channel A.

If the Stokes vector of light going into Channel A is $[S_0, S_1, S_2, S_3]^T$, then the light coming out $S_{out} = [S_0, S_1, S_2, S_3]^T$ can be expressed as

$$\begin{bmatrix} S_0' \\ S_1' \\ S_2' \\ S_3' \end{bmatrix} = LP(90) \cdot CR2(45) \cdot CR1(0) \cdot \begin{bmatrix} S_0 \\ S_1 \\ S_2 \\ S_3 \end{bmatrix} \quad (3)$$

where *LP (90)* is the Mueller matrix of polarizer at 90 degrees, *CR2 (45)* and *CR1 (0)* are the Mueller matrix of the two crystals with fast axis at 45° and 0° respectively. S_0' is the only quantity of the outgoing light that we can measure and thus we need to make a series of measurements that vary S_0'.

After expanding Eq. (3) and substituting Eq. (2) for σ and solving for S_0' we have

$$S_0' = S_0 - S_1 \cdot Cos(\frac{V_2 \cdot \pi}{V_{\pi 2}}) - S_2 \cdot Sin(\frac{V_1 \cdot \pi}{V_{\pi 1}}) \cdot Sin(\frac{V_2 \cdot \pi}{V_{\pi 2}}) + S_3 \cdot Sin(\frac{V_2 \cdot \pi}{V_{\pi 2}}) Cos(\frac{V_1 \cdot \pi}{V_{\pi 1}}) \quad (4)$$

Where $V_{\pi 1}$ and $V_{\pi 2}$ are the half-wave voltages of the two LiNOb3 crystals, calibrated to be 623 V and 685V respectively, and V_1 and V_2 are the voltages applied on the crystals.

Equation (4) shows that S_0' will modulate with the voltages applied on the two crystals and S_0' can be measured. Therefore, Stokes vector of the incoming light, $[S_0, S_1, S_2, S_3]$, can be solved as a function of V_1, V_2 and S_0'. However, when we applied light with known Stokes vectors to validate the technique, the output S_0' does not behave as predicated by Eq. (4). For example, we generated horizontal polarized light and Stokes vector of this light were computed as $[1, 0.9937, -0.0079, 0.0185]^T$ through channel B. However the Stokes vector computed using channel A was $[1, 0.7597, 0.1417, -0.5251]^T$. Two possible reasons were:

a) The two crystals were not aligned perfectly with the optical axis. Slight misalignments can cause a relatively large phase shift along the crystal, leading to polarization

#132430 - $15.00 USD Received 29 Jul 2010; revised 18 Sep 2010; accepted 19 Sep 2010; published 30 Sep 2010

rotation if the alignment is not exactly parallel or perpendicular to the polarization. While we performed the alignment carefully, we cannot rule out that this was a problem.

b) Manufacturer issues: it is possible that the electrodes of the two crystals were not perfectly parallel with the z axis of the EO crystals, causing the electrical field axis to be at a slight angle with the optical axis of the crystals. This would result in a small deviation in the modulation from the theoretical prediction.

2.2.2 Inverse Matrix Method

To bypass this limitation, we introduced an algorithm to back compute the behavior of the crystals as a function of known input lights. Suppose the polarization properties of the two EO crystals and polarizer can be collectively represented by a matrix X. Equation (4) can be modified as Eq. (5)

$$I_{out} = X \cdot S \tag{5}$$

where I_{out} is the intensity of light going through channel A, X is the matrix describing the polarization properties of the crystals, and S is the Stokes vector of the incident light. If we can determine matrix X by experiment, then S can be calculated as a function of I_{out} as

$$S = (X^T \cdot X)^{-1} \cdot X^T \cdot I_{out} \tag{6}$$

Theoretically, the 4 elements of the Stokes vector can be calculated from 4 measurements of I_{out}, and the size for matrix X only needs to be 4 x 4. In order to increase accuracy, we chose to over-sample and perform a least squares fit. This was desirable, because there is a tradeoff between the number of measurements and the accuracy of the fit. Using a model eye we performed a number of trial experiments to decide how many measurements we should make. As expected, more measurements increased the accuracy, but increasing the number of samples would either decrease the image size of the retina or if we increase the imaging time to compensate would increase the probability of eye motion induced errors. We converged on 7 measurements as a compromise between accuracy and retinal image size. The use of seven measurements required us to scan a single line 7 times with different voltages on the two crystals. The resultant matrix size was therefore 7 x 4. With the line scan rate of our system at 8 kHz, we could form Stokes vector line images at more than 1kilolines/sec.

The setup for measuring matrix X is shown in Fig. 1. A plane mirror was placed in the retinal conjugate plane of the AOSLO system to reflect light into the AOSLO, and into Channels A and B. A quarter wave plate and a half wave plate were used to generate light of different polarization states. The APD detector in channel A was replaced by a 10 mHz adjustable balanced receiver (New Focus) to record the intensity of light. In channel B, a QW polarization analyzer (a rotatable 1/4 wave plate followed by a polarizer and a detector) was used to measure the Stokes vector of the same light. Before calibrating the system, the polarization properties of light at spot A and B were confirmed to be identical by separate polarization state measurements. Lights with 30 different polarization states were used for the calibration. These thirty different polarized lights were generated by rotating a quarter wave plate or half waveplate in front of the plane mirror. To improve the calibration accuracy, the thirty lights were generated such that their Stokes vectors were spread across the Poincare sphere. For each input, we varied the voltage on the two EO crystals from −360 V to 360 V in 120 V steps (7 values). 210 equations were generated, and the least-square fit was performed to determine matrix X. The result is shown as Eq. (7):

#132430 - $15.00 USD Received 29 Jul 2010; revised 18 Sep 2010; accepted 19 Sep 2010; published 30 Sep 2010

$$X = \begin{bmatrix} 147.433 & -111.486 & -101.538 & 16.97494 \\ 147.9548 & -45.9059 & -132.504 & 41.47455 \\ 145.5168 & 50.14756 & -75.4786 & 78.30778 \\ 146.9625 & 113.4901 & 24.14714 & 38.84631 \\ 151.8327 & 127.2029 & 37.66345 & -48.7225 \\ 152.5378 & 116.4572 & -44.066 & -70.461 \\ 144.8684 & 101.4427 & -92.8547 & 2.152597 \end{bmatrix} \quad (7)$$

To verify the accuracy of X, we inverted the process. We used the matrix X and the 30 measured intensities to back calculate the corresponding 30 Stokes vectors. As expected, the computed Stokes vectors agreed well with the actual ones used in the calibration.

2.3 Verifying EO polarimeter performance

To verify the calibration, an additional 25 lights of different polarization states from those used in calibration were generated and measured by channel B (Fig. 1). For each input, we varied the voltages on the EO crystals from −360 V to 360 V in 120 V steps (7 values). The Stokes vector of the light was then determined by Eq. (6). Intraclass correlation analysis and ANOVA analysis were used to test if the Stokes vector measured by the QW and the EO methods agreed.

2.4 AOSLO System calibration

The polarization properties of the AOSLO were calibrated in 2 steps: First, a QW polarization analyzer was placed at the exit pupil of the system. The Stokes vector of the incident light was confirmed to be linearly polarized. Second, a plane mirror was placed at the retinal conjugate plane of an artificial eye at the exit pupil of the system. The light returning from the plane mirror was measured using channel B. The resultant Stokes vector of the light after passing the double-pass imaging system was calculated as $[1,-0.9775, -0.064, 0.0226]^T$, DOP was computed to be 0.98, within experimental error of the ideal value of 1.0.

2.5 Scanning mode modification

The AOSLO used a horizontal scanning frequency of 8 kHz with a vertical frame scan of 15 Hz controlled by a D/A converter. We reprogrammed the vertical scanner to generate different vertical scanning patterns. For conventional intensity imaging, each line was displaced vertically by approximately 1 micron. For polarization imaging, the vertical scan progresses as usual for the first 112 lines to form a regular image, which helps us recognize the area being imaged on the retina when testing a subject. Then the vertical scanner is stopped and the same horizontal line is swept 7 times by the horizontal scanner. During this period, the voltage on the EO crystals was modulated from −360 V to + 360 V in 120 V step, synchronized to the line rate. Then the vertical scan is moved down 1 micron and the same scanning pattern was performed on the next 7 sweeps. In this case, we scanned an area with 57 lines with 7 different polarization states for each line. Figure 2 compares an intensity image A, and a polarization scanning image B.

#132430 - $15.00 USD Received 29 Jul 2010; revised 18 Sep 2010; accepted 19 Sep 2010; published 30 Sep 2010

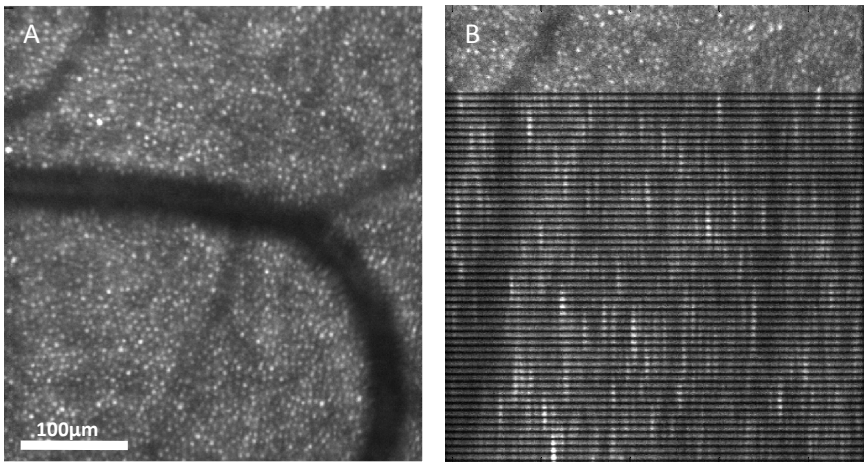

Fig. 2. Images from different imaging mode of the AOSLO. (A) Regular scanning image; (B) Polarization scanning image. Scale bar is 100 μm. Images were collected at 5 degrees on nasal retinal from subject1.

2.6 Image processing

All images were acquired using a 200 μm confocal aperture (4 x the size of the Airy disc). This somewhat large confocal aperture allowed us to collect not only the polarized light returning from the retina but also the scattered light, which is more depolarized. 50 sequential image frames were recorded during each image collecting section in about 3 seconds. Offline image processing requires that we first select a number of good frames (less eye motion, good image quality), and align and average the frames using custom MATLAB programs (MathWorks, Inc.). A group of 7 images corresponding to 7 different voltages on two LiNOb3 crystals were generated. Cross correlation was calculated in the brightest group images at 8 different locations. Centroid of the cross correlations was used to determine the location of best alignment, generating sub-pixel accuracy. Images were then aligned using an approach similar to that of Stevenson and Roorda [45]. The alignment was performed for those detection channel states which produced the highest intensity, and the other 6 conditions were moved accordingly. This allowed us to avoid alignment errors that result from aligning very dim images. Figure 3 shows the 7 reconstructed images after aligning and averaging (40 frames).

2.7 DOP calculation for individual cone photoreceptors

After the images were aligned and Stokes vector images were computed, individual cone photoreceptors of each subject were located manually in the intensity image. The DOP of each cone photoreceptors was calculated.

#132430 - $15.00 USD Received 29 Jul 2010; revised 18 Sep 2010; accepted 19 Sep 2010; published 30 Sep 2010

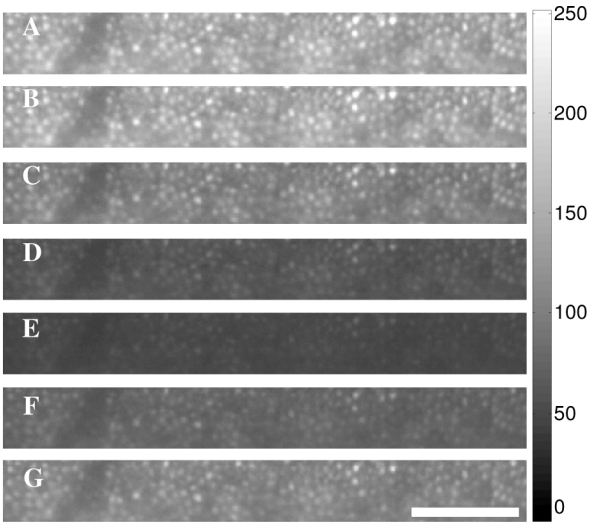

Fig. 3. Reconstructed images with different voltages on the two EO crystals. (A) −360 V, (B) −240 V, (C) −120 V, (D) 0 V, (E) 120 V, (F) 240 V, (G) 360 V. Scale bar is 100 μm.

2.8 Subjects

Three healthy subjects (2 males and one female; age range 24-26 years, mean 25) participated in this study. All subjects have received a complete eye examination and all of them had best corrected visual acuity of 20/20 or better. Pupils were dilated with 0.5% tropicamide during data collection. Pupil size was at least 6 mm in a darkened room. A three axis chin rest and forehead pads were used to positioning the subjects' pupil with the system pupil to get the best quality images. Informed consent forms were obtained after a full explanation of the procedures and consequences of this study. This study protocol was approved by Indiana University Institutional Review Board and complied with the requirements of the Declaration of Helsinki.

3. Results

3.1 Dual EO Polarimeter Performance

Figure 4 plots the S_1, S_2, S_3 and DOP of the 25 polarized lights measured in the verification phase of the experiment by the QW polarization analyzer and the EO polarization analyzer. A 2-way ANOVA revealed no statistical significant difference between the individual Stokes vectors measured with the two techniques, $p = 0.967$. We computed the intraclass correlation coefficients between the two polarization techniques and found excellent agreement Correlations for S_1, S_2, S_3 and DOP were 0.996, 0.936, 0.982 and 0.701 respectively, $p < 0.001$. To test the repeatability, a model eye was imaged using this Dual EO AOSLO polarimeter at different times (5 minutes interval) and Stokes vector images of this model eye were computed at each time point. Normalized cross correlation was performed on the S_1, S_2, S_3 and DOP images at different time, the correlations between these Stokes vector images at different time are over 96% for all 4 parameters.

3.2 Polarization images of cone photoreceptors from healthy subjects

To test the ability of the dual EO polarimeter to make measurements *in vivo*, polarization images from 3 young healthy subjects were acquired using the dual LiNOb3 crystal channel with the Indiana AOSLO. Light illuminating the eye was set to be vertically polarized. To improve the signal to noise ratio of images, thirty to forty images (slightly more than 2 seconds) for each polarization setting were aligned and averaged and the Stokes vectors calculated. Figure 5 shows Stokes vectors images at 5 degrees in the nasal retina of subject 1.

#132430 - $15.00 USD Received 29 Jul 2010; revised 18 Sep 2010; accepted 19 Sep 2010; published 30 Sep 2010

Figure 6 shows the calculated Stokes vector of cone photoreceptors normalized according to the intensity at each location (Stokes vector images). From the Stokes vector images, we also computed the normalized S0 image, the DOP image and the DODP image. We found the cone photoreceptors showed higher polarization preservation than the structures around them. Blood vessel shadows showed less polarization preservation presumably because the light was multiply scattered. These results agree with those from a previous study [40].

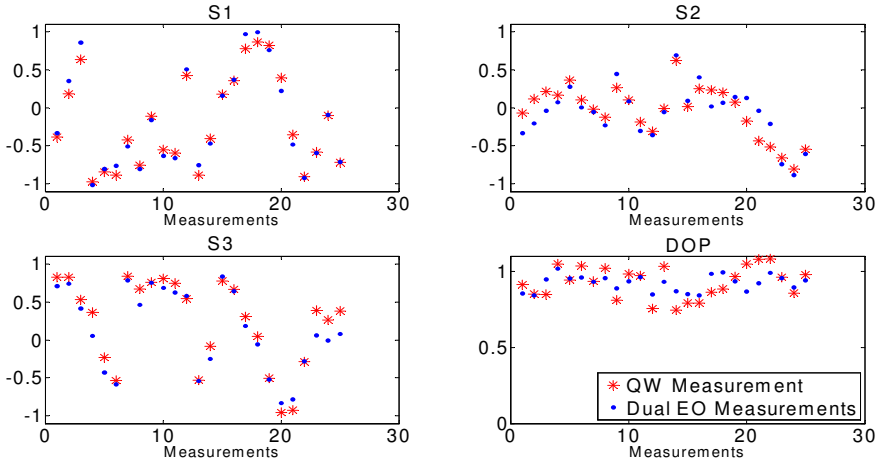

Fig. 4. Comparison of Stokes vector and DOP measured with two polarization techniques.

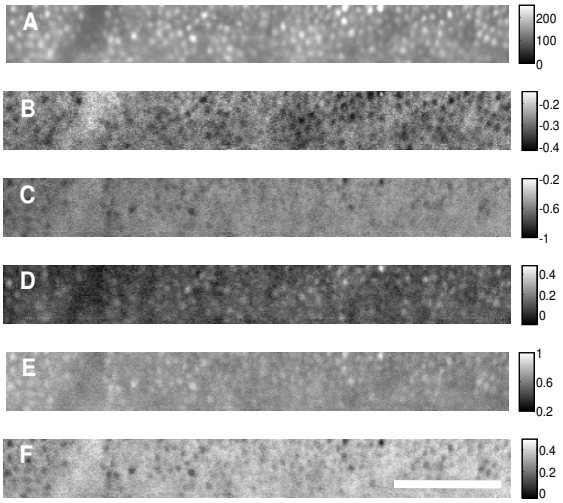

Fig. 5. Computed Stokes vector images at 5° nasal retina from Subject1. A. Intensity image (S_0). B. S_1 image. C. S_2 image. D. S_3 image. E. Degree of polarization (DOP) image. F. Degree of depolarization (DODP) image. The gray-level code is showed at the right side. Scale bar is 100 μm.

#132430 - $15.00 USD Received 29 Jul 2010; revised 18 Sep 2010; accepted 19 Sep 2010; published 30 Sep 2010

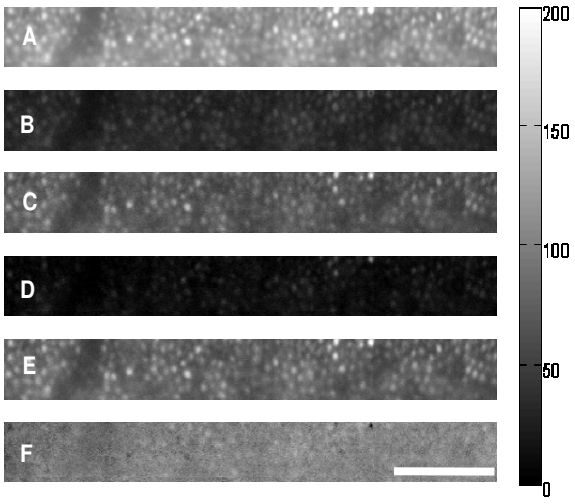

Fig. 6. Result from the same subject as in Fig. 5. A. Intensity images for all light (S_0). B. S_0*S_1 image. C. S_0*S_2 image. D. S_0*S_3 image. E. All polarized light (S_0 *DOP). F. All depolarized light (S_0 *DODP). All of the images are formed using absolute intensity value. Scale bar is 100 µm.

3.3 Degree of polarization of individual cone photoreceptors

The degree of polarization of individual cone photoreceptors was calculated (Fig. 7) as a function of intensity of cone photoreceptors for all 3 subjects. Statistical analysis revealed a significant correlation between the degree of polarization and the intensity of the cone photoreceptor ($p < 0.001$) with brighter cones having a higher degree of polarization.

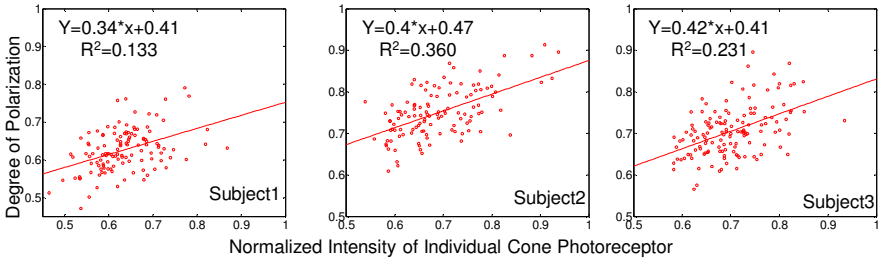

Fig. 7. Correlation between cone photoreceptor intensity and degree of polarization. Data are from 3 subjects. All regression slopes are statistically significant, $p < 0.0001$.

3.4 Polarization images of nerve fiber layer from healthy subjects

Our new polarimeter can also be used to measure variations in polarization properties for other retinal structures. Figure 8 shows an image of the nerve fiber layer from subject 2. Panel A shows the nerve fiber layer 6 degree in the nasal retina. Panel B shows the Stokes vector of nerve fiber layer normalized according to the intensity at each location (Stokes vector images). All images are formed using absolute values.

4. Discussion and Conclusion

Polarization techniques have been previously used to improve contrast in biological imaging [14,16,27,46–48]. In a previous study [40], we described a technique to analyze the Stokes vector of light returning from cellular structures of the retina by combining a quarter waveplate polarization analyzer with an AOSLO. The error introduced by eye movements was

#132430 - $15.00 USD Received 29 Jul 2010; revised 18 Sep 2010; accepted 19 Sep 2010; published 30 Sep 2010

a major problem for that technique. In the present study, we replaced the quarter waveplate analyzer with dual EO crystals. EO crystals have the capability to change their birefringence linearly with the electrical field at mega hertz frequencies [49]. In our case we modulated them at 8 kHz. Using this approach we were able to acquire polarization data from individual lines at a rate of 1.17 kHz and a pixel rate of more than 580 kilo_vectors/sec. Time between two lines is only about 0.88 ms, therefore the error caused by the eye movement within a line is negligible. The effect of eye movement and tear film on the image intensity will be reduced.

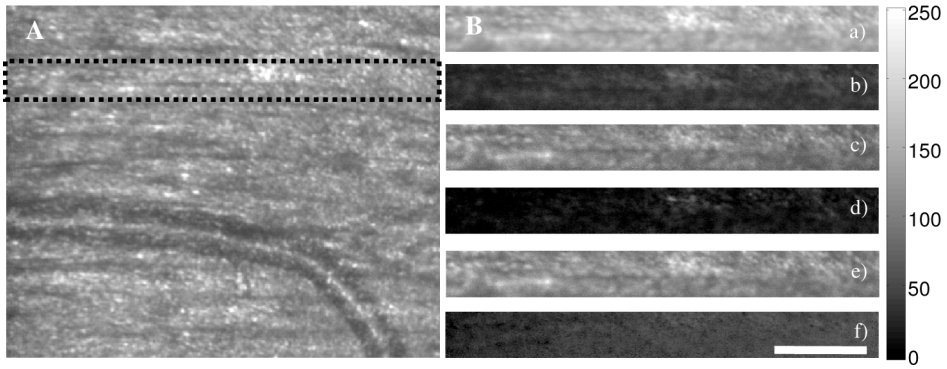

Fig. 8. Images of nerve fiber layer of subject 2 at 6 degree nasal retina. Different structures showed different polarization properties. Scale bar is 100 μm. Region in dash line in panel A is where the polarization images in B are computed. In panel B, (a) intensity image, (b) S_1*intensity, (c) S_2*intensity, (d) S_3*intensity, (e) DOP*intensity, f) DODP*intensity. Images in panel B is the region in the dashed line in panel A.

Alignment of the electro-optical modulators proved to be critical and we could not count on arriving at perfectly aligned crystals. Small misalignment of the crystals can cause a large phase shift across the long axis of the crystal. We consider it most likely that slight misalignments caused errors when we followed the conventional method for operating the systems. These slight phase errors the caused the Stokes vector measurements to be inaccurate when compared to a waveplate polarimeter. To circumvent the problem, we used an inverse method to empirically determine the polarization matrix of the crystals as a function of voltage using a set of known Stokes vectors as inputs. With this algorithm, even in the presence of slight misalignment or imperfections with these crystals, the condition number of the inverse matrix is adequate to quickly and accurately calculate matrix X and use it to calculate the Stokes vector of the incident light. Our data showed that the QW polarization analyzer and the EO polarization analyzer calibrated in this manner produced statistically identical Stokes vector measurement of the same incident light.

The major factor affecting the measured individual differences in the overall Stokes vector of light returned from the retina probably arise from corneal birefringence. Studies have shown that in most corneas, the slow axis pointed nasally downward [2,50]. Spatial variation of birefringence of cornea has also been indicated in some studies [1,51,52]. In our study, Stokes vector images of retinal structures not only represent the polarization properties of the retinal structures, they also include the polarization information from the cornea. However, our entire scan angle is only about 1.6 degrees, and so the variation of corneal polarization across this field should be small. The cornea will affect the overall image, but not comparisons across cells. Nevertheless we did measure variations in the polarization state between cones. This can be seen when we plot the Stokes vectors of individual cone photoreceptors at 5 degree in the nasal retina for each of the 3 subjects (Fig. 9). Stokes vector of cone photoreceptors of each subject clumped together at different locations, presumably depending on the corneal birefringence. Within a single subject's data the cones varied somewhat in terms of both their depolarization and their polarization angle.

#132430 - $15.00 USD Received 29 Jul 2010; revised 18 Sep 2010; accepted 19 Sep 2010; published 30 Sep 2010

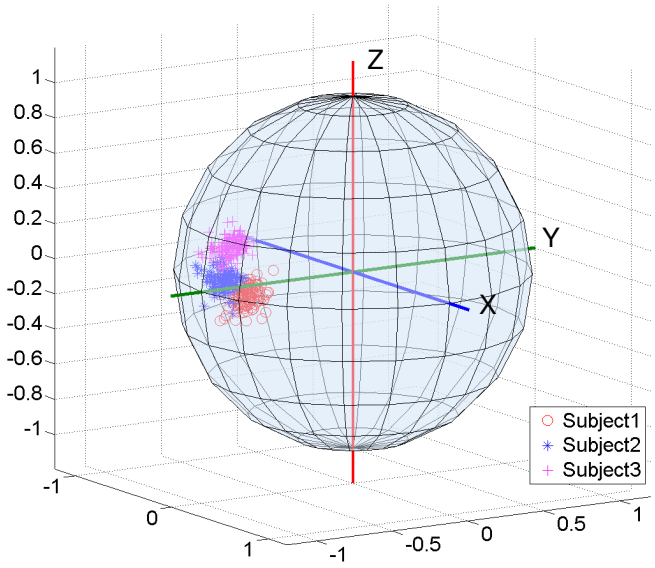

Fig. 9. Stokes vectors of individual cone photoreceptors were plotted on the Poincare sphere.

The variation between cones in a single subject probably has at least two sources. First, there should be differences locally due to variations in retinal birefringence (such as the nerve fiber layer) and also due to differences between cones. Again because the field size is small, the variation across the field, which arises from nerve fiber layer birefringence, should be small particularly for this region of the retina where the fibers tend to be aligned in a common direction and show little local curvature. The second possibility for individual differences in DOP is associated with the fact that the light from the cones appears to be the light scattered within the cones and guided back towards the pupil. It is well known that the cones are directionally tuned, a property known as the Stiles-Crawford effect [53–56]. It has been shown [57,58] that the portion of light guided by the photoreceptors retains its polarization, while light that has been scattered more widely did not. Simple mixing of the scattered and guided components of light predicts that cone photoreceptors with higher intensity should have higher degree of polarization, as we measured. Using just the portion of the light that maintains polarization greatly increases the contrast of the cone images. In comparison, the shadows of blood vessels are illuminated by a higher proportion of multiply scattered light and therefore have a higher DODP. The final possibility is that there are slight differences between cones in their birefringence, although confirming this will require future experiments.

In summary, we developed a high speed high resolution retinal polarimeter. Using this polarimeter, we are able to measure the Stokes vector of light returning from different structures of retina at the cellular level. Compared with our previous study, this new technique has the advantage of higher speed, higher accuracy, and less prone to eye movement errors. The technique can be used to improve the retinal image contrast of different retinal structures and distinguish them based on their polarization properties. It has the potential to be used as a clinical tool to help detect and quantify early retinal changes associated with aging, age-related maculopathy, and age-related macular degeneration.

Acknowledgments

This work was supported by the National Institutes of Health (NIH) EY04395, EY14375 and P30EY019008. We thank Toco Yuenping Chui for help with data collection and Yanming Zhao for discussions on data analysis. We thank Ann Elsner, Brian Marks and Don Miller for constructive feedback on the manuscript.

#132430 - $15.00 USD Received 29 Jul 2010; revised 18 Sep 2010; accepted 19 Sep 2010; published 30 Sep 2010